ACS Catalysis

Research Article

Cite This: ACS Catal. 2018, 8, 10606−10618

pubs.acs.org/acscatalysis

# Cobalt Pincer Complexes in Catalytic C−H Borylation: The Pincer Ligand Flips Rather Than Dearomatizes

Haixia Li,[†] Jennifer V. Obligacion,[‡] Paul J. Chirik,[‡] and Michael B. Hall*,[†]

[†]Department of Chemistry, Texas A&M University, College Station, Texas 77843, United States

[‡]Department of Chemistry, Princeton University, Princeton, New Jersey 08544, United States

Supporting Information

**ABSTRACT:** The mechanism for the borylation of an aromatic substrate by a cobalt pincer complex was investigated by density functional theory calculations. Experimental observations identified *trans*-($^{iPr}$PNP)-$CoH_2$(BPin) as the resting state in the borylation of five-membered heteroarenes and 4-BPin-($^{iPr}$PNP)Co($N_2$)BPin as the resting state in the catalytic borylation of arene substrates. The active species, 4-R-($^{iPr}$PNP)-CoBPin (R = H, BPin), were generated by reductive elimination of $H_2$ in the former, through Berry pseudorotation to the cis isomer and $N_2$ loss in the latter. The catalytic mechanism of the resulting Co(I) complex was computed to involve three main steps: C−H oxidative addition of the aromatic substrate ($C_6H_6$), reductive elimination of PhBPin, and regeneration of the active complex. The oxidative addition product formed through the most favorable pathway, where the breaking C−H bond of $C_6H_6$ is parallel to a line between the two phosphine atoms, leaves the complex with a distorted PNP ligand, which rearranges to a more stable complex via dissociation and reassociation of HBPin. Alternative pathways, $\sigma$-bond metathesis, and the oxidative addition in which the breaking C−H bond is parallel to the Co−B bond are predicted to be unlikely for this Co(I) complex. The thermodynamically favorable formation of the product PhBPin via reductive elimination drives the reaction forward. The active species regenerates through the oxidative addition of $B_2Pin_2$ and reductive elimination of HBPin. *In the overall reaction, the flipping (refolding) of the five-membered phosphine rings, which connects the species with two phosphine rings folded in the same direction and that with them folded in different directions, is found to play an important role in the catalytic process, as it relieves steric crowding within the PNP ligand and opens Co coordination space.* Metal−ligand cooperation based on the ligand's aromatization/dearomatization, a common mechanism for heavy-metal pincer complexes, and the dissociation of one phosphine ligand do not apply in this system. This study provides guidance for understanding important features of pincer ligands with first-transition-row metals that differ from those in heavier metal complexes.

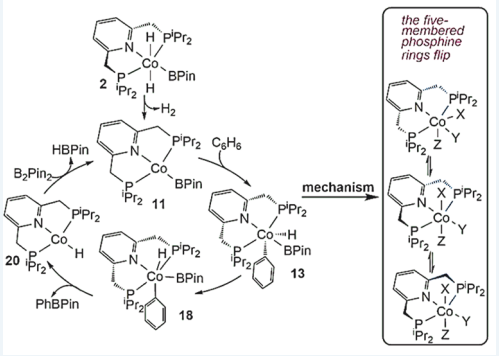


**KEYWORDS:** *cobalt pincer complex, catalytic C−H borylation, flipping of the five-membered phosphine rings, DFT calculations, mechanistic studies*



## 1. INTRODUCTION

Catalytic C−H borylation is one of the most attractive methods for C−H functionalization, as the C−B products are versatile synthetic reagents for constructing new carbon−carbon and carbon−heteroatom bonds.[1] Efforts by many researchers have developed catalytic borylations for C($sp^3$)−H, C($sp^2$)−H,[1−6] C(sp)−H bonds,[7−11] and chemo-, regio-, and stereoselective C−H borylations.[1−4,9−11] Among them, catalytic C−H borylation of arenes and heteroarenes is a particularly attractive approach to synthesize organoboronate esters, which are key synthetic intermediates for Suzuki−Miyaura cross-coupling reactions.[1−6]

Transition-metal complexes have been widely applied to catalyze the C−H borylations, for which the iridium-based complexes are most common.[1−5,8] Furthermore, some iridium complexes have been reported to catalyze methane borylations,[12,13] a major challenge. However, widespread applications for iridium and other noble metal catalysis suffer from their many disadvantages: expense, toxicity, scarcity, and difficulty in separation. These limitations have motivated researchers to develop catalysts with earth abundant first transition-row metals,[14,15] paving the way for sustainable and environmentally friendly synthesis. Although Hartwig and co-workers reported several C−H borylations with $CpFe(CO)_2$Bcat (Cp = $\eta^5$-$C_5H_5$; cat = $O_2C_6H_4$) under photochemical conditions in 1995, catalytic reactions were not observed in their systems.[16] Significant progress in developing catalytic C−H borylations with first transition-row metal complexes has only been made recently. Although catalytic C−H borylations has been reported by using metal-free systems based on the concept of "Frustrated Lewis Pairs",[17−21] most of the work has involved bimetallic copper−iron[22−24] and zinc−iron complexes,[22,23]

Received: August 6, 2018
Revised: September 30, 2018
Published: October 17, 2018




DOI: 10.1021/acscatal.8b03146
ACS Catal. 2018, 8, 10606−10618

monometallic iron complexes,[25−27] and recently a series of cobalt[28−35] and nickel complexes.[36,37]

Important applications of C−H borylations in synthetic chemistry need new efficient catalysts, whose development can benefit from fully understanding the catalytic mechanism. Such mechanisms at various level of detail have been reported from both experiments and computations.[20,23,33,34,38−45] Furthermore, efforts to elucidate the origin of chemo-, regio-, and stereoselectivity have also had some success.[4,46−54] Generally, catalytic borylations involve C−H bond cleavage by oxidative addition and C−B bond formation by reductive elimination, routes that utilize the inherent two-electron redox properties of heavier transition metals. However, metal-assisted $\sigma$-bond metathesis mechanism has been suggested for the C−H bond cleavage and H transfer,[39,42,45,47,49] a route that avoids the formation of higher oxidation-state intermediates. In addition, both steric and electronic effects, together with weak interactions between ligands and substrates, were found to govern the selectivity of some reactions.[47,49,50,54]

Despite of these studies, detailed mechanistic investigations of C−H borylations with first transition-row metals are still scarce.[20,43] Unlike heavier transition metals with two-electron redox chemistry, the first-row metals usually demonstrate one-electron redox processes,[14,15] a difference that suggests that some new mechanistic pathways may be involved. Furthermore, variable coordination geometries and multiple spin states of the first transition-row metal complexes, especially those with weak field ligands, challenge characterizations of their electronic structures and catalytic reactivity. Thus, metal−metal cooperativity has been recognized to facilitate the catalytic photochemical C−H borylation with bimetallic Cu−Fe and Zn−Fe complexes, which may mimic heavier transition metal complexes.[22−24] Herein, we are interested in understanding the catalytic mechanism for the C−H borylations of heterocycles and arenes with several pincer-ligated cobalt complexes reported by Chirik and co-workers.[28] Among their tested cobalt complexes, the pyridine-based PNP pincer complex, ($^{iPr}$PNP)Co($CH_2SiMe_3$) ($^{iPr}$PNP = 2,6-bis(di-iso-propyl)phosphinomethyl)pyridine, **1** in Scheme 1), was observed to perform best. With the catalyst **1**, the borylation of methyl furan-2-carboxylate has achieved up to 5000 turnovers at 23 °C (eq 1 in Scheme 1), and the borylation of benzene has also been realized with excess benzene (benzene:$B_2Pin_2$ = 20:1, Pin = $O_2C_2Me_4$) at 80 °C (eq 2 in Scheme 1). The trans-

**Scheme 1. Cobalt Pincer Complex 1 and Its Catalyzed Borylation Reactions**

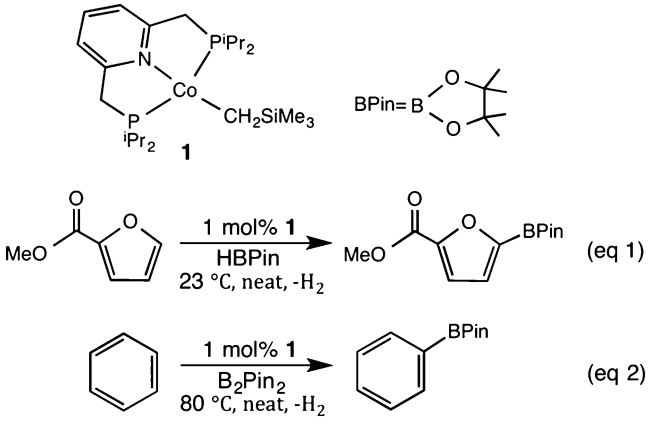


dihydride cobalt complex, *trans*-($^{iPr}$PNP)$CoH_2$(BPin) (Pin = $O_2C_2Me_4$, complex **2** in Figure 1), synthesized separately by

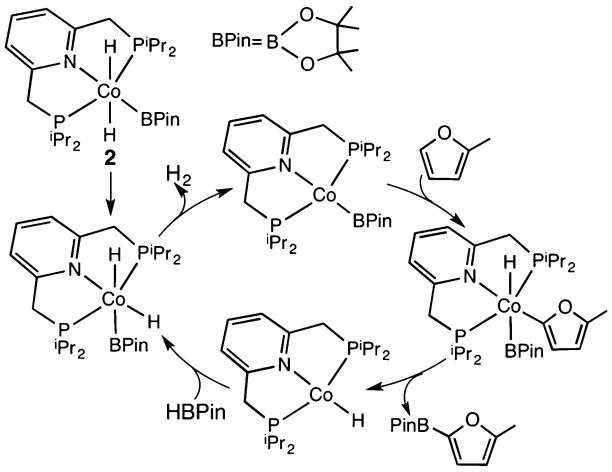


**Figure 1.** Proposed mechanism for the catalytic borylation of 2-methylfuran with HBPin from the resting-state complex **2** in ref 28.

adding 2 equiv of HBPin to the cobalt alkyl compound **1** and releasing 1 equiv of $Me_3SiCH_2BPin$, was identified as the resting state in the borylation of 2-methylfuran with HBPin. According to their proposed mechanism (Figure 1), complex **2** first isomerizes to a *cis*-dihydride cobalt complex, which then releases $H_2$ to generate the active species ($^{iPr}$PNP)CoBPin, followed by the oxidative addition of a C−H bond and the subsequent reductive elimination of the B−C bond to form the borylated product. Finally, addition of HBPin to ($^{iPr}$PNP)CoH regenerates complex **2**. Although several experiments have been conducted to explore the catalytic mechanism and the structures of cobalt intermediates,[28−34,55] a complete catalytic cycle has not been established yet. Furthermore, related PNP pincer ligated metal complexes synthesized by Milstein and co-workers are well-known to show a mode of metal−ligand cooperation based on the ligand's aromatization/dearomatization.[56−58] This gives rise to an interesting question that whether the *trans*-($^{iPr}$PNP)$CoH_2$(BPin) complex shows similar reactivity or not during its catalytic cycle. Building on our previous mechanistic studies of the borylation with transition metal complexes[39,42,48] and studies of Milstein's systems,[58,59] we herein employed density functional theory (DFT) calculations to fully understand the catalytic mechanism by computing the detailed reaction pathways for the proposed mechanism as shown in Figure 1.

## 2. COMPUTATIONAL METHODS

Detailed DFT calculations of the catalytic mechanism were conducted by using benzene and $B_2Pin_2$ as representative substrates with catalyst **1** (eq 1 in Scheme 1), as all its C−H bonds are equal, benzene simplifies our explorations on the mechanism. With the $\omega$B97XD functional,[60] geometries of all intermediates and transition states were optimized in gas phase by employing the basis set BS1, where atoms of the $^{iPr}$PNP ligand except N and P use cc-pVDZ[61] and the others (including the Co) use Def2TZVP.[62] On the basis of gas-phase optimized geometries, single point calculations were conducted in $C_6H_6$ solvent with the SMD solvent model[63] at the level of $\omega$B97XD/Def2TZVP, where all the atoms use Def2TZVP. In addition, an "ultrafine" grid was used to make



DOI: 10.1021/acscatal.8b03146
ACS Catal. 2018, 8, 10606−10618

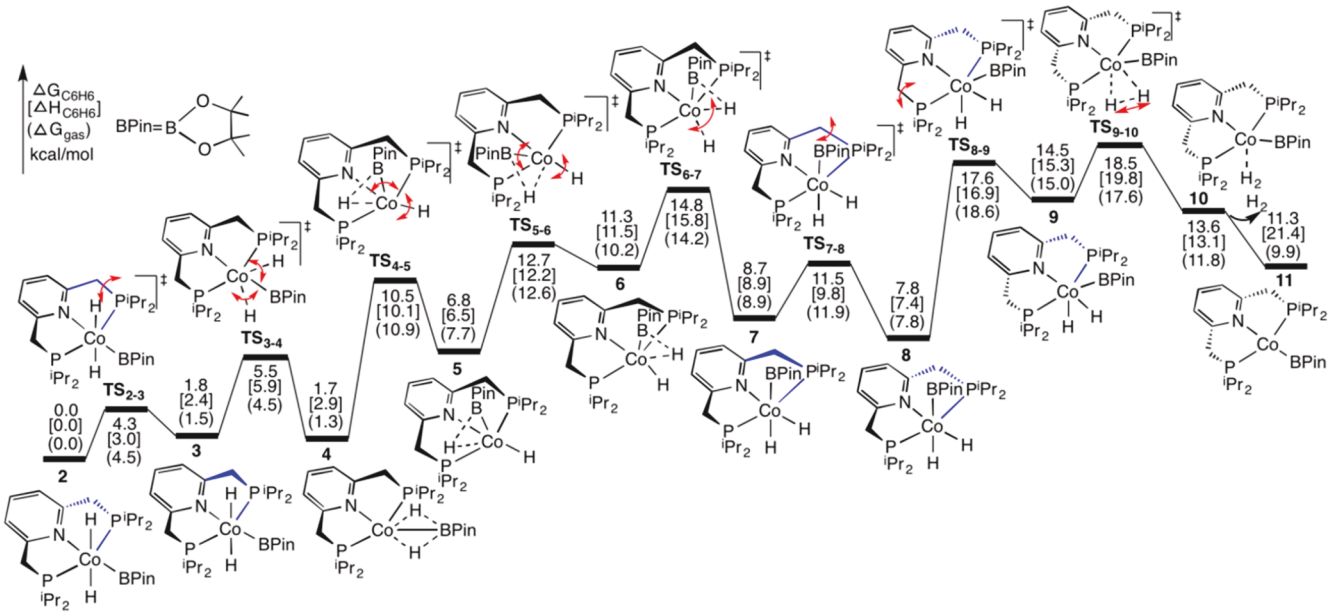


**Figure 2.** Calculated energy profiles for the release of $H_2$ from *trans*-($^{iPr}$PNP)$CoH_2$(BPin) complex **2**, which isomerizes to *cis*-($^{iPr}$PNP)$CoH_2$(BPin) before the rate determining reductive elimination.

optimizations of large molecules with many soft modes such as methyl rotations more reliable. Furthermore, the "5D" option was used for all d functions in these calculations. Unless noted otherwise, free energies and enthalpies in $C_6H_6$ solvent together with the free energies in gas phase, which are represented by $\Delta G_{C6H6}[\Delta H_{C6H6}](\Delta G_{gas})$, respectively, are reported in this work.

In addition to calculating the experimentally reported system, we also computed a simplified model system to explore various alternative reaction pathways. In the simplified model system, we replaced all the iPr substituents of the $^{iPr}$PNP ligand with Me and further replaced $B_2Pin_2$ with $B_2eg_2$ (eg = ethylene glycolato) to save computation time. The $\omega$B97XD functional was also used to calculate the model system. Geometries of all intermediates and transition states were optimized in gas phase at the level of BS2, where Co employs LANL2DZ ECP-basis set[64] and the others use cc-pVDZ. With the optimized geometries in gas phase, the energetic results were refined by single point calculations with the SMD solvent model at the level of $\omega$B97XD/BS3, where Co employs SDD ECP-basis set[65] and the others use cc-pVTZ. The THF solvent, which was used in the catalytic borylation of some substituted pyridines in experiments, was selected in the SMD single point calculations. Free energies and enthalpies in THF and the free energies in gas phase, which are represented by $\Delta G_{THF}[\Delta H_{THF}](\Delta G_{gas})$, were reported. Results for the model system are presented mainly in the Supporting Information.

Results reported in this work are based on optimized geometries for closed shell singlet states. However, triplet states or open shell singlet states may also be possible for cobalt complexes, especially for four-coordinate cobalt species. For example, the solid-state structure of the cobalt alkyl complex **1** was confirmed to be diamagnetic with a four-coordinate Co in a square-planar geometry, while its $^1$H NMR spectra appears to be somewhat paramagnetically shifted at high temperature, implying a low-lying triplet state.[28] To verify this observation, several DFT functionals involving hybrid functionals ($\omega$B97XD, M06,[66] TPSSh[67]) and nonhybrid functionals (TPSS,[67] TPSS-D3 (with D3 = Empirical Dispersion = GD3BJ[68]), M06L,[69] PBE[70]) were selected to calculate its possible structures. As expected, the relative energies between singlet and triplet states depend strongly on the functionals, where TPSS gives square-planar, singlet ground states and $\omega$B97XD over stabilizes tetrahedral triplet states (SI1). To further confirm this, several experimentally isolated species, ($^{iPr}$PNP)CoCl, ($^{tBu}$PNP)CoCl, and ($^{tBu}$PNP)-CoH,[55] were investigated by using TPSS and $\omega$B97XD. Similarly, TPSS predicts singlet ground states consistent with experiment, while $\omega$B97XD over stabilizes triplet states (SI1). Comparisons of the optimized geometries at TPSS and $\omega$B97XD show that $\omega$B97XD predicts longer Co−X bonds (X = any coordinated atom) than TPSS, and these differences are larger for triplet states than for singlet states (SI1). With TPSS, singlet and triplet states of selected stationary points, especially the four-coordinate cobalt species involved in the reaction, such as ($^{iPr}$PNP)CoBPin (**11**), ($^{iPr}$PNP)CoPh (**16**), and ($^{iPr}$PNP)CoH (**20**), were recalculated, and all are predicted to be singlet ground states (SI1). Thus, the singlet states are reported for the mechanism. The geometries and the energies reported for the reaction mechanism are from the $\omega$B97XD calculations, as their predicted rate-determining barriers (around 25 kcal/mol) are more consistent with the experimental conditions at 80 °C than the barriers of over 34 kcal/mol predicted by using the TPSS functional (see the following discussions). However, using TPSS to recalculate the rate-determining transition states and thermodynamics of key steps did not change the conclusions.

All the DFT calculations were performed with the Gaussian 09 program.[71] The three-dimensional molecular structures reported in this work were drawn using the JIMP2 molecular visualizing and manipulating program.[72−74]

## 3. RESULTS AND DISCUSSION

Following the proposed mechanism of catalytic borylation of 2-methylfuran with HBPin from the *trans*-($^{iPr}$PNP)-



DOI: 10.1021/acscatal.8b03146
ACS Catal. 2018, 8, 10606−10618

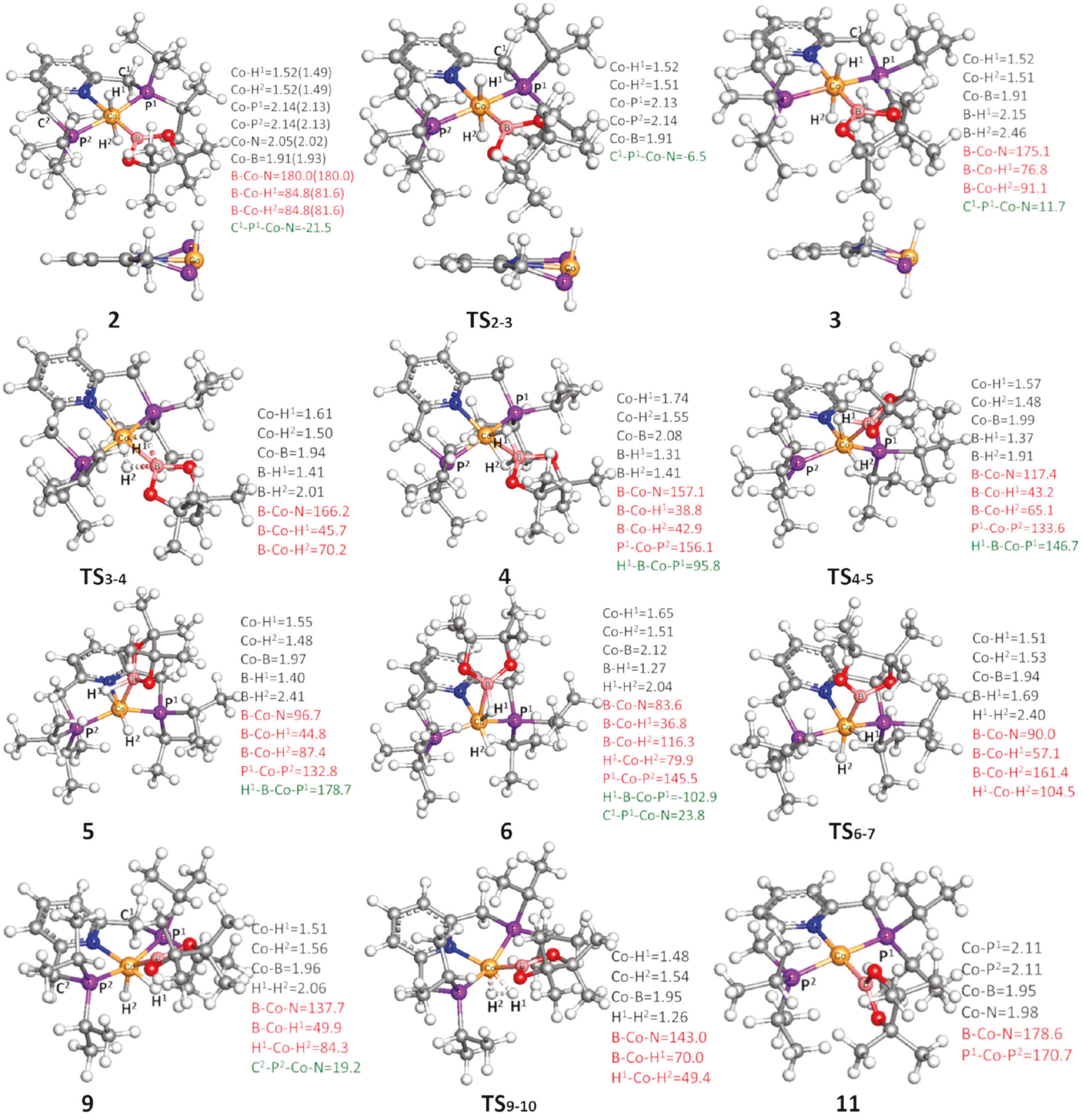


**Figure 3.** Optimized geometries of key species involved in the mechanism in Figure 2 (other species are in SI2). Some bond distances in angstroms, angles in degrees, and dihedral angles in degrees are given in black, red, and green colors, respectively. Values in the parentheses in complex **2** are from its crystal structure. Geometries of **2**, $\mathbf{TS}_{2-3}$, and **3** drawn in another perspective are also shown here, where iPr groups on P and BPin on Co are omitted for clarity.

$CoH_2(BPin)$ complex (**2**, a resting state in the reaction) as in Figure 1,[28,34] the active species ($^{iPr}$PNP)CoBPin was generated from the *trans*-($^{iPr}$PNP)$CoH_2$(BPin) complex by releasing $H_2$. Furthermore, in the catalytic borylation of arene substrates, the 4-BPin-($^{iPr}$PNP)Co($N_2$)BPin complex (BPin substituted the 4-position of the pincer ligand) was identified as the resting state, which was proposed to form the related active species 4-BPin-($^{iPr}$PNP)CoBPin through the dissociation of $N_2$.[30] From the active species, the catalytic borylation mechanism involves similar steps: oxidative addition of the C−H bond, reductive elimination of B−C bond, and regeneration of the active species. We first examined the mechanism for the generation of the active species ($^{iPr}$PNP)CoBPin from the *trans*-($^{iPr}$PNP)-$CoH_2$(BPin) complex to determine if aromatization/dearomatization of the pincer ligand is operative in this system or not. Then, we calculated the following three steps from the active species ($^{iPr}$PNP)CoBPin by using $C_6H_6$ and $B_2Pin_2$ as substrates to reduce the computational cost: oxidative addition of $C_6H_6$, reductive elimination of B−C bond to form PhBPin, and regeneration of ($^{iPr}$PNP)CoBPin. Considering that 4-BPin-



DOI: 10.1021/acscatal.8b03146
*ACS Catal.* 2018, 8, 10606−10618

($^{iPr}$PNP)CoBPin is the active species in the catalytic borylation of arene substrates, some selected transition states and intermediates involved in the oxidative addition and reductive elimination steps were recalculated by using the 4-BPin-($^{iPr}$PNP)CoBPin complex. Details for these steps will be reported separately in the following sections.

**3.1. Generation of ($^{iPr}$PNP)CoBPin from *trans*-($^{iPr}$PNP)-$CoH_2$(BPin).** In the experiments, the *trans*-($^{iPr}$PNP)-$CoH_2$(BPin) complex **2** was observed as a resting state in the catalytic reaction and was proposed to release $H_2$ to generate an active species ($^{iPr}$PNP)CoBPin.[28,34] However, direct release of $H_2$ from **2** is unlikely as the two H atoms on Co are trans. Thus, an isomerization process from **2** to a *cis*-($^{iPr}$PNP)$CoH_2$(BPin) complex was suggested.[28] Our calculations support this suggestion, and the detailed pathway for this process is shown in Figure 2 with optimized geometries of some species in Figure 3.

The optimized geometry of complex **2** is close to its X-ray crystal structure, as the differences of bond lengths and angles between them are no more than 0.03 Å and 3.2°, respectively (see Figure 3 and their superimposed structures in SI3), an agreement that supports the methodology used here. In **2**, two five-membered phosphine rings of the pincer ligand are folded in different directions; one $sp^3$-C of the ring tips down (in blue), while the other tips up (in black). Via transition state $\mathbf{TS_{2-3}}$, the $sp^3$-C of the phosphine ring in blue flips up, and a new complex **3** was formed. This ring-flipping process is clear from their optimized geometries and is especially obvious from the alternative perspective in Figure 3. The two hydrides at Co are trans in **3**, and then move simultaneously toward the B atom via transition state $\mathbf{TS_{3-4}}$ where the Co−$H^1$ bond lengthens and both B−H distances shorten, generating complex **4** with two unequally bridging H atoms (Co−H−B) (see its optimized geometry in Figure 3). In contrast, the stepwise pathway where the two hydrides move separately is unlikely; as optimizations of corresponding intermediates formed after moving one hydride repeatedly converge to **3** again. Complex **4** is higher than **2** by only 1.7 kcal/mol, and the formation of **4** from **2** is calculated to proceed via two low-barrier transition states, $\mathbf{TS_{2-3}}$ and $\mathbf{TS_{3-4}}$. In addition, an alternative pathway for the formation of **4** from **2**, where the two hydrides at Co in **2** first move simultaneously toward the B atom and then the $sp^3$-C of the phosphine ring in blue flips up to generate **4**, was calculated to compete with the path in Figure 2 (see SI4). Furthermore, a dynamic process was suggested by experiments, which show a broad cobalt hydride signal in $^1$H NMR spectrum.[28] Thus, this experimental observation can be ascribed to the rapidly transformation between **2** and **4** which represent a *mer* isomer and a *fac* isomer, respectively, the latter also displaying semibridging Hs.

In the optimized geometry of **4** (Figure 3), the N, Co, and B atoms are not in line with the BPin group bending upward. In addition, the B−$H^1$ bond is shorter than the B−$H^2$ bond by 0.10 Å, implying that the B atom is bound to $H^1$ more tightly than to $H^2$. Correspondingly, the Co−$H^1$ bond is longer than the Co−$H^2$ bond by 0.19 Å. Furthermore, the B−$H^1$ bond at 1.31 Å and the Co−$H^2$ bond at 1.55 Å are in the normal range for these bonds. Thus, complex **4** could be considered the product formed by coordinating $H^1$BPin to a cobalt-hydride complex (i.e., **20** in the following sections). Consistent with this proposal, a process for the dissociation of HBPin from an isomer of complex **4**, where two five-membered phosphine rings of the pincer ligand are folded in different directions, has been located with a barrier of 12.4 kcal/mol higher than **4**. Therefore, the $H^1$BPin group in **4** is able to rotate in a counterclockwise direction along the B−Co axis toward $P^1$ and simultaneously $H^2$ moves far from B, as is described by $\mathbf{TS_{4-5}}$, to form complex **5**, which adopts a distorted trigonal bipyramidal geometry in which $H^1$BPin and phosphine ligands occupy the equatorial positions with $H^2$ and pyridine ligands in the axial positions. Subsequently, the $H^1$BPin group of **5** continues to rotate in an anticlockwise direction along the B−Co axis toward $H^2$, and concurrently $H^2$ moves downward (i.e., far from the B atom) via transition state $\mathbf{TS_{5-6}}$, giving complex **6**, which adopts a distorted trigonal bipyramidal geometry in which $H^2$, $H^1$BPin, and pyridine ligands occupy the equatorial positions with phosphine ligands lying almost in the axial positions. Here, we are considering $H^1$BPin as a single $\sigma$-bonded ligand with $H^1$−B bond occupying one coordination site, although both $H^1$ and B are shown as coordinated to Co in Figure 3. Thus, the isomerization process from **4** to **6** via **5** proceeds like a Berry pseudorotation,[75] which occurs widely in trigonal bipyramidal structures. Compared to **4**, the B−$H^2$ distance is longer and the $P^1$−Co−$P^2$ angle is smaller in **5** (Figure 3); thus, **5** is higher in energy due to the loss of the B−$H^2$ bonding interaction and the steric effects of two phosphine ligands in **5**. Furthermore, **6** is higher than **5** because of additional steric effects between $H^2$, $H^1$BPin, and pyridine ligands in the same plane. For the same reasons, the barrier of $\mathbf{TS_{5-6}}$ is also higher than that of $\mathbf{TS_{4-5}}$.

The two hydrides, which in **6** are cis with $H^1$ bridging Co and B atoms, then simultaneously move away from B (via $\mathbf{TS_{6-7}}$) to generate **7**. Complex **7** adopts an octahedral geometry with one H trans to N and the other trans to B, and the two five-membered phosphine rings in **7** are folded in the same direction. Next, one $sp^3$-C of the phosphine ring (in blue) flips down via $\mathbf{TS_{7-8}}$ to form complex **8**, *cis*-($^{iPr}$PNP)-$CoH_2$(BPin), which is more stable than **7** but less stable than the *trans*-($^{iPr}$PNP)$CoH_2$(BPin) complex **2** by 7.8 kcal/mol. Then in $\mathbf{TS_{8-9}}$ the other phosphine ring (in black) is also flipping down to form **9**, in which the BPin group is bending toward the trans position of the pyridine ligand because of steric clashes with the P substituents. The movement of BPin drives the H atoms closer and the $H_2$-formation transition state, $\mathbf{TS_{9-10}}$, leads to an $H_2$ $\sigma$-complex, **10**, which then releases $H_2$ to generate a four-coordinated Co(I) complex **11** with a planar geometry around Co. The formation of **11** has been confirmed in experiments by capturing it as a CO adduct, **11(CO)**, with CO occupying a vacant position on Co.[30] It should be noted that the five-membered ring plane of BPin is perpendicular to the plane of the pyridine ring in the optimized geometry of **11**. In contrast, the two planes are parallel to each other in the crystal structure of **11(CO)**. Comparisons of the Co−X bonds (X = any coordinated atom) in the optimized geometry and crystal structure of **11(CO)** show that the largest difference (0.023 Å) corresponds to the Co−N bond. When CO is added to the structure of **11**, BPin rotates toward being planar, but there is a barrier to overcome to form the planar **11(CO)**; however, the planar structure is more stable than this intermediate structure. Furthermore, optimizations of the structure generated by removing CO from **11(CO)** converge back to the geometry of **11** in Figure 3. In the process for the release of $H_2$ from **2** (Figure 2), the rate-determining transition state is $\mathbf{TS_{9-10}}$ with a barrier of 18.5[19.8](17.6) kcal/mol, and the formation of **11** and $H_2$ is uphill by 11.3[21.4](9.9) kcal/mol relative to complex **2**. The TPSS functional predicts a


DOI: 10.1021/acscatal.8b03146
ACS Catal. 2018, 8, 10606−10618

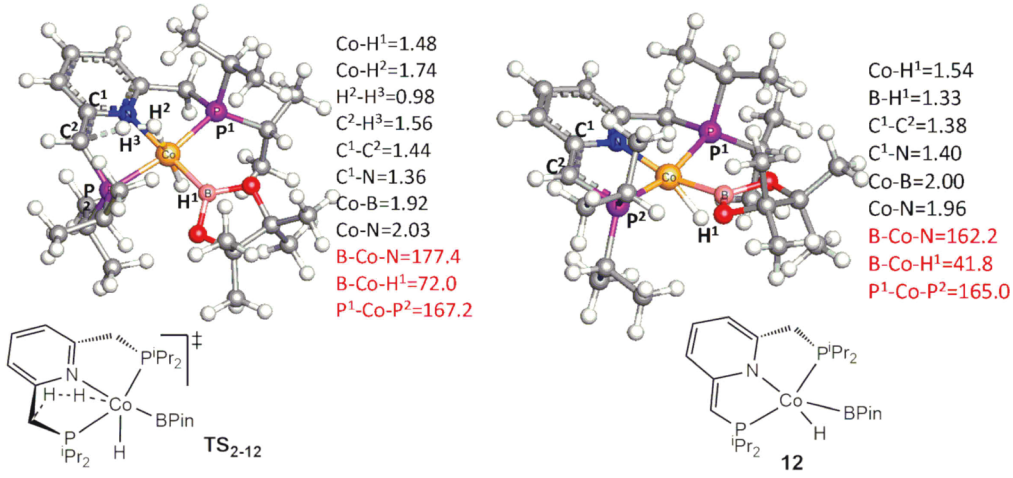


**Figure 4.** Optimized geometries of transition state $\mathbf{TS_{2-12}}$ and complex **12**. Some bond distances in angstroms and angles in degrees are given in black and red colors, respectively.

more favorable process, where the barrier for $\mathbf{TS_{9-10}}$ and the products **11** and $H_2$ are 15.2[16.2](16.2) and 6.5[16.8](16.2) kcal/mol, respectively.

In the reverse reaction complex **9** can be considered an $H_2$-activation product that is formed from **11** and $H_2$ via $\mathbf{TS_{9-10}}$, where the $H_2$ bond-breaking H atoms are moving toward BPin and pyridine ligands, respectively. Alternatively, $H_2$ can be also cleaved along a direction parallel to the line between two phosphine atoms to form an isomer of **9**, which adopts an octahedral geometry in which two H atoms and two phosphine ligands occupy the equatorial positions, and the pyridine ligands and BPin occupy the axial positions. As shown in SI5, this isomer of **9** could be formed reversibly, which then releases $H_2$ to regenerate complex **11**.

For each species in Figure 2, several different geometries are possible by rotating iPr groups of the phosphine ligands, and the geometries shown in Figure 3 and SI2 correspond to the most stable ones. In addition, these geometries are considered to isomerize between each other very easily by rotating the iPr groups separately (see SI6 for an example of the isomerization process from **4** to its isomer). Thus, species with different orientations of iPr groups may exist, but that would not change the results obtained in the following discussions.

The mechanism shown in Figure 2 is generally similar to that for the model systems (SI7), in which all the iPr substituents of the $^{iPr}$PNP ligand were replaced with Me and $B_2Pin_2$ was replaced with $B_2eg_2$ (superscript "m" is added to the reported complex's number to denote their corresponding model complex). Due to less steric clashing between the substituents on the phosphine ligands in the model systems, the barriers for the ring "flipping" transition states $\mathbf{TS_{2-3}}^{\mathbf{m}}$, $\mathbf{TS_{7-8}}^{\mathbf{m}}$, and $\mathbf{TS_{8-9}}^{\mathbf{m}}$ are 2.6, 8.0, and 16.5 kcal/mol relative to $\mathbf{2}^{\mathbf{m}}$ (Figures S5 and S6), which are lower than the corresponding (full system) transition states $\mathbf{TS_{2-3}}$, $\mathbf{TS_{7-8}}$, and $\mathbf{TS_{8-9}}$ in Figure 2. By using the model systems, other possibilities were checked. For example, the isomerization between $\mathbf{11}^{\mathbf{m}}$ and its isomer in which two five-membered phosphine rings are folded in different directions was calculated to occur very easily (Figure S6). Furthermore, isomers of $\mathbf{5}^{\mathbf{m}}$, $\mathbf{6}^{\mathbf{m}}$, and $\mathbf{10}^{\mathbf{m}}$ in which two five-membered phosphine rings are folded in different directions are found to be unlikely, as optimizations of these isomers repeatedly converge to $\mathbf{5}^{\mathbf{m}}$, $\mathbf{6}^{\mathbf{m}}$, and $\mathbf{10}^{\mathbf{m}}$, respectively. In addition, other possible pathways are calculated to be unlikely or less favorable, which include the direct release of $H_2$ from the cis-dihydride cobalt complex $\mathbf{8}^{\mathbf{m}}$, the formation of $\mathbf{8}^{\mathbf{m}}$ from the trans-dihydride cobalt complex $\mathbf{2}^{\mathbf{m}}$ via the dissociation and association of HBeg (Figure S7), the formation of $\mathbf{8}^{\mathbf{m}}$ from $\mathbf{2}^{\mathbf{m}}$ through dissociation of one phosphine (Figure S8), and the release of $H_2$ via the dearomatization of the pyridine ligand (Figure S9). Our results, which involve reductive elimination (RE) of $H_2$ from a Co(III) pincer complex, differ from a previous study of the C−C bond formation via RE from a cobalt(III) dimethyl complex, where dissociation of a phosphine ligand was required prior to RE.[76] Maybe for future work, it is also interesting to compare the PNP system with all of this flexibility to terpyridine ones that also borylate but are more rigid.

Among these unfavorable pathways, the dearomatization of the pyridine ligand is quite interesting, as a series of PNP pincer ligated Ru complexes that are similar to complex **2** have been synthesized by Milstein and co-workers and reported to show a mode of metal−ligand cooperation based on the ligand's aromatization/dearomatization.[56−58] Pincer ligand benzylic deprotonations and hydrogen abstractions in related Co(I) complexes suggest that the metal−ligand cooperation in the Rh complexes may involve deprotonation at the benzylic site,[55] consistent with calculations on the Ru mechanism.[56−58] To confirm the conclusions obtained with model systems, we recalculated this pathway by using complex **2** with the full ligand ($^{iPr}$PNP). Considering that the pyridine ligand and other atoms use different basis sets in the optimizations (see SI1 in Computational Methods), we employed another basis set BS4 (LANL2DZ for Co and 6-31G* for the others) to optimize the species involved in this pathway. The rest of the methodology was the same (see Computational Methods). Thus, the results for this pathway used in the following discussions are obtained at the level of ωB97XD/Def2TZVP(SMD)//ωB97XD/BS4. At this level, the barrier for $\mathbf{TS_{9-10}}$ and the product complex **11** with the release of $H_2$ are 18.2[19.5] and 10.7[21.3] kcal/mol ($\Delta G_{C6H6}$[$\Delta H_{C6H6}$]), respectively, relative to **2**. As shown in SI8, the level of ωB97XD/Def2TZVP(SMD)//ωB97XD/BS4 is suitable in the calculations of this system by giving reasonable optimized geometries and the results close to that at the level of ωB97XD/Def2TZVP(SMD)//ωB97XD/BS1.



DOI: 10.1021/acscatal.8b03146
ACS Catal. 2018, 8, 10606−10618

**Table 1. Results for the Release of $H_2$ at the Level of $\omega$B97XD/Def2TZVP(SMD)//$\omega$B97XD/BS4[a]**

| R | $TS_{9-10}^{R}$ | $11^{R} + H_2$ | $TS_{2-12}^{R}$ | $12^{R} + H_2$ |
|---|---|---|---|---|
| | 18.2[19.5](17.2) | 10.7[21.3](4.8) | 31.5[32.4](32.0) | 6.1[17.1](5.0) |
| Ir | 32.5[34.4](31.8) | 17.4[28.8](16.3) | 36.8[36.8](39.0) | 14.3[24.3](18.1) |
| Ph | 19.1[20.5](18.0) | −0.6[11.6](−7.8) | 28.9[29.3](28.7) | 6.3[17.6](7.5) |
| Ir_Ph | 35.0[34.5](35.7) | 9.1[20.1](8.3) | 34.2[34.2](36.2) | 12.1[22.7](17.2) |
| Ir_Ph_tBu | 41.5[45.9](42.6) | 9.0[20.0](8.2) | 33.5[34.1](35.5) | 10.9[22.1](15.5) |

[a]Values in kilocalories per mole are $\Delta G_{C6H6}[\Delta H_{C6H6}](\Delta G_{gas})$ and are relative to $2^{R}$, respectively.

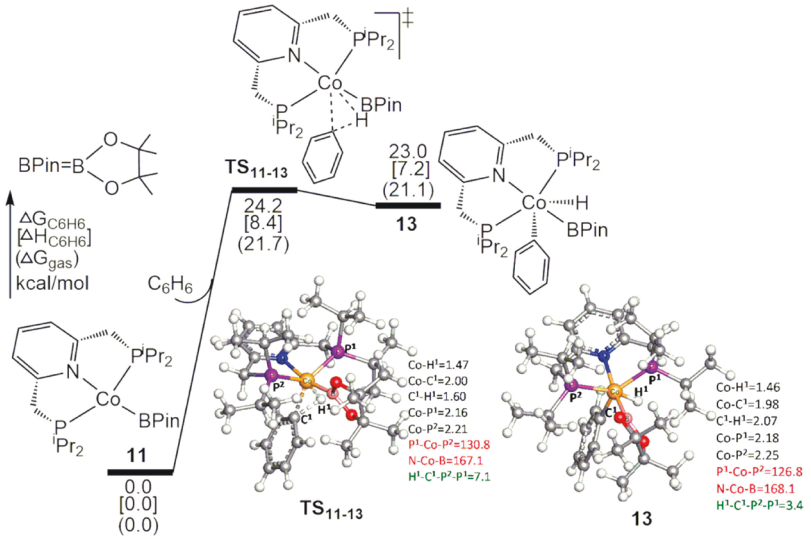


**Figure 5.** Calculated energy profiles for the oxidative addition of $C_6H_6$ to **11**. Some bond distances in angstroms, angles in degrees, and dihedral angles in degrees are given in black, red, and green colors, respectively.

With $\omega$B97XD/BS4, the optimized geometries for transition state $TS_{2-12}$ and the product complex **12** involved in the pathway via the dearomatization of the pyridine ligand are shown in Figure 4. $TS_{2-12}$ corresponds to the formation of $H_2$ by eliminating a hydride at Co and a proton from the $sp^3$-C of the pyridine ligand. In contrast to the reductive elimination pathway to form the Co(I) complex **11** via $TS_{9-10}$, complex **12** remains a Co(III) complex due to the dearomatization of the pyridine ligand. In addition, the hydride at Co is close to B, which could indicate an interaction between the hydride and the vacant orbital on B. At the level of $\omega$B97XD/Def2TZVP-(SMD)//$\omega$B97XD/BS4, $TS_{2-12}$ and complex **12** with the release of $H_2$ are 31.5[32.4] and 6.1[17.1] kcal/mol ($\Delta G_{C6H6}[\Delta H_{C6H6}]$), respectively, relative to **2**. In addition, the dissociation of HBPin from **12** is unfavorable, as this process is endothermic by 13.1[27.4] kcal/mol. The origin of the higher barrier for $TS_{2-12}$ can be seen in the distance between two eliminating H atoms in their optimized geometries. The distance between the hydride at Co and the hydrogen atom at $sp^3$-C of the pyridine ligand decreases by 2.02 Å in forming $TS_{2-12}$, the corresponding distance between the two eliminating H atoms decreases by only 0.82 Å in forming $TS_{9-10}$. Thus, changing geometries from **2** to $TS_{2-12}$ requires more energy. Moreover, the dearomatization of the pyridine ligand further destabilizes transition state $TS_{2-12}$. Therefore, the mechanism for the release of $H_2$ via the dearomatization of the pyridine ligand is less favorable than that via the reductive elimination mechanism shown in Figure 2. Furthermore, the mechanism via the reversible ligand dearomatization-aromatization was also ruled out based on the experimental observations.[30]

To understand the effect of the metal, we investigated the release of $H_2$ from the corresponding iridium complex $\mathbf{2}^{Ir}$ (*trans*-($^{iPr}$PNP)Ir$H_2$(BPin)) formed by replacing Co in **2** with Ir. The barriers for $H_2$ formation in the iridium analogues are higher than those in the cobalt systems: $TS_{9-10}^{Ir}$ and $TS_{2-12}^{Ir}$ are higher than $TS_{9-10}$ and $TS_{2-12}$ by 14.3 and 5.3 kcal/mol, respectively (Table 1). To understand the effect of the ligand, we also calculated the release of $H_2$ from their phenyl analogues ($\mathbf{2}^{Ph}$ = *trans*-($^{iPr}$PNP)Co$H_2$(Ph) and $\mathbf{2}^{Ir\_Ph}$ = *trans*-($^{iPr}$PNP)Ir$H_2$(Ph)), which are generated by using Ph to replace BPin in **2** and $\mathbf{2}^{Ir}$, respectively. The barriers for $H_2$ formation for **2** and $\mathbf{2}^{Ir}$ are close to those for their phenyl analogues ($\mathbf{2}^{Ph}$ and $\mathbf{2}^{Ir\_Ph}$) with the variations of less than 3 kcal/mol (Table 1). Thus, the choice of the metal affects the reactivity to a greater degree than the choice of the ligand. In particular, the barriers for $H_2$ formation via the reductive elimination mechanism for iridium analogues ($TS_{9-10}^{Ir}$ and $TS_{9-10}^{Ir\_Ph}$) are higher by more than 14 kcal/mol than those for cobalt systems ($TS_{9-10}$ and $TS_{9-10}^{Ph}$, respectively). In contrast, $H_2$ formation via the dearomatization of the pyridine ligand for the iridium analogues ($TS_{2-12}^{Ir}$ and $TS_{2-12}^{Ir\_Ph}$) are higher by only 5.3 kcal/mol than those for the cobalt systems ($TS_{2-12}$ and $TS_{2-12}^{Ph}$, respectively). Relative to $\mathbf{2}^{Ir}$, the barriers for the $H_2$ formation, $TS_{9-10}^{Ir}$ and $TS_{2-12}^{Ir}$, are over 32 kcal/mol (Table 1). Consistent with these results, Chirik and co-workers observed that the iridium congener with a pyrrolidinyl substituent in 4-position of the pincer ligand is very stable under catalytic conditions, which can be ascribed to a more difficult reductive elimination from Ir(III) to Ir(I) than from Co(III) to Co(I), as proposed by Chirik and co-workers.[30] Furthermore, Milstein and co-workers did not observe the


DOI: 10.1021/acscatal.8b03146
ACS Catal. 2018, 8, 10606−10618

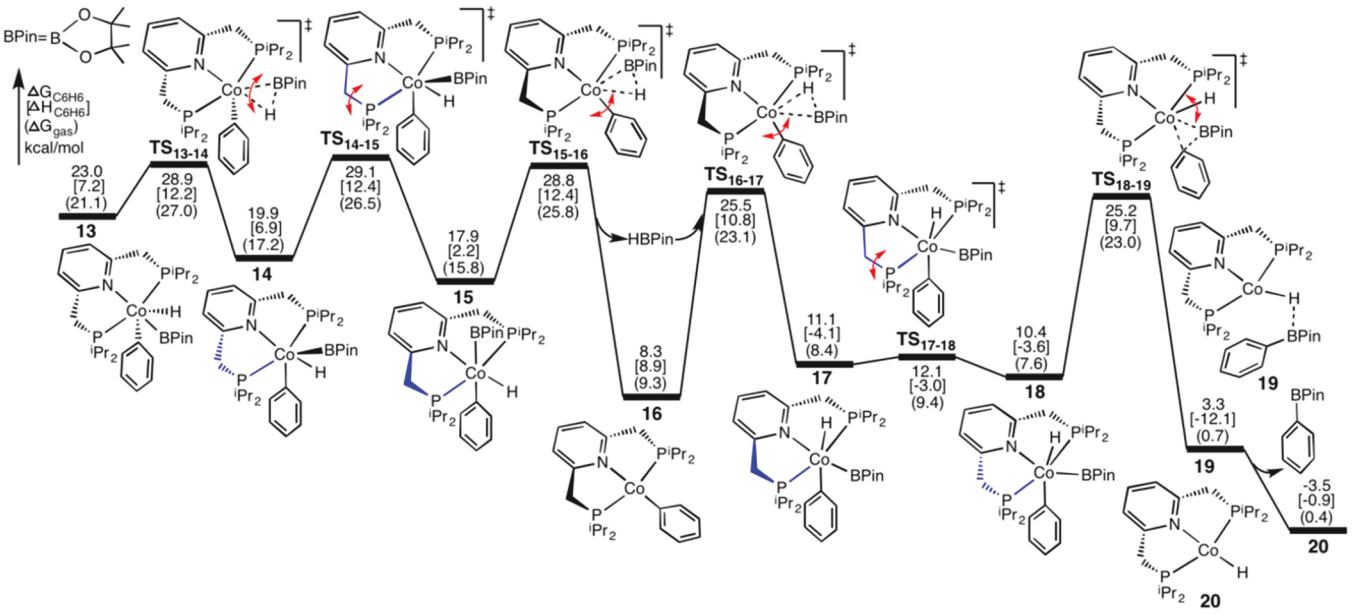


**Figure 6.** Calculated energy profiles for the reductive elimination of B−C bond to form PhBPin. The energies for these species are relative to separate $C_6H_6$ and **11**, and their optimized geometries are shown in SI14.

release of $H_2$ from an iridium complex $\mathbf{2}^{\mathbf{Ir\_Ph\_tBu}}$ (*trans*-($^{tBu}$PNP)Ir$H_2$(Ph)),[77] for which the predicted barriers for $H_2$ formation are over 33 kcal/mol (Table 1). In addition, $\mathbf{TS_{2-12}}^{\mathbf{Ir\_Ph\_tBu}}$ is very close to $\mathbf{TS_{2-12}}^{\mathbf{Ir\_Ph}}$, while $\mathbf{TS_{9-10}}^{\mathbf{Ir\_Ph\_tBu}}$ is much higher than $\mathbf{TS_{9-10}}^{\mathbf{Ir\_Ph}}$, which can be ascribed to the steric effects between tBu groups in $\mathbf{TS_{9-10}}^{\mathbf{Ir\_Ph\_tBu}}$ (see their optimized geometries in SI9).

**3.2. Oxidative Addition of $C_6H_6$.** The cobalt boryl complex ($^{iPr}$PNP)CoBPin (**11**), which is generated from complex **2** via the $H_2$ release mechanism (Figure 2), is the active species that catalyzes the borylation reactions of five-membered heteroarenes. This active species can also be formed in the presence of $B_2Pin_2$ directly from the catalyst precursor ($^{iPr}$PNP)Co($CH_2SiMe_3$) (**1**) by releasing $Me_3SiCH_2BPin$, as observed in experiments.[28] This reaction was calculated to be thermodynamically very favorable ($\Delta G_{C6H6}[\Delta H_{C6H6}](\Delta G_{gas})$ = −25.1[−24.6](−27.3) kcal/mol), and a possible pathway with reasonable barriers was located by using the model systems (SI10). The calculated energy profiles for the oxidative addition of $C_6H_6$ by **11** together with their optimized geometries are shown in Figure 5. A search along the backward direction of the imaginary frequency from $\mathbf{TS_{11-13}}$ toward **11** failed to find either a Co $\sigma$-complex or a Co $\pi$-complex. In the forward direction of the oxidative-addition transition state $\mathbf{TS_{11-13}}$, the breaking C−H bond of $C_6H_6$ is parallel to a line between the two phosphine atoms. Thus, $\mathbf{TS_{11-13}}$ adopts a distorted TBP geometry in which $C_6H_6$ and the phosphines occupy equatorial positions, while the pyridine and BPin occupy axial positions. In distorted octahedral geometry of the product, **13**, the PNP ligand occupies one face of the octahedron around Co, while $C_6H_5$, H, and BPin occupy the other face. Therefore, due to the distorted backbone of pyridine ligands and the steric effects between the substituents of phosphine ligands, complex **13** is very high in energy, 23.0 kcal/mol relative to separated **11** and $C_6H_6$. This step is also unfavorable under the TPSS functional, where $\mathbf{TS_{11-13}}$ and **13** are 34.8[18.9](19.5) and 33.6[18.2](18.8) kcal/mol, respectively. However, the next process, the reductive elimination of B−C bond to form PhBPin, can drive the overall reaction forward.

In addition to the pathway shown in Figure 5, alternative pathways for the oxidative addition of $C_6H_6$ to the cobalt boryl complex in the model systems were explored (SI11): (1) an oxidative-addition pathway to form another facial isomer of $\mathbf{13}^{\mathbf{m}}$ in which $C_6H_5$ and Beg are switched (Figure S13(B) in SI11), (2) oxidative-addition pathways directly forming meridional complex $\mathbf{15}^{\mathbf{m}}$ (see Figure 6 and Figure S13(C) in SI11) and its meridional isomer in which $C_6H_5$ and H are switched (Figure S13(D) in SI11), (3) $\sigma$-bond metathesis pathways, and (4) a pathway for the oxidative-addition of $C_6H_6$ to the cobalt complex with one phosphine ligand dissociated (Figure S14 in SI11). However, these alternative pathways were calculated to be unlikely or less favorable than that in Figure 5.

Some conclusions obtained from the model systems remain the same for the experimentally reported systems (SI12). For example, alternative $\sigma$-bond metathesis pathways remain unlikely relative to oxidative addition, because the Co(I) in **11** is easily oxidized to Co(III) via the oxidative addition. In contrast, previously reported $\sigma$-bond metathesis pathways are proposed for the reactions of complexes in high oxidation states, such as W(III),[39,45] Rh(III),[42] and Ir(III)[47,49] complexes. In addition, alternative oxidative-addition pathways to form meridional complex **15** and its meridional isomer are still less favorable than that via $\mathbf{TS_{11-13}}$ in Figure 5 (Figure S15 in SI12). The lower barrier of $\mathbf{TS_{11-13}}$ can be ascribed to lower distortion energy of the Co catalyst and the more negative interaction energy (Table S6 in SI12).

Using model complexes, pathways for adding $C_6H_6$ to the corresponding Rh and Ir complexes ($\mathbf{Rh11}^{\mathbf{m}}$ and $\mathbf{Ir11}^{\mathbf{m}}$) obtained by replacing Co in $\mathbf{11}^{\mathbf{m}}$ with Rh and Ir, respectively, were examined (SI13). Like the Co complex, $\sigma$-bond metathesis pathways for the Rh and Ir complexes are still unlikely because of their low oxidation states. In addition, the oxidative-addition pathways via $\mathbf{RhTS_{11-13}}^{\mathbf{m}}$ and $\mathbf{IrTS_{11-13}}^{\mathbf{m}}$ (corresponding Rh and Ir transition states of $\mathbf{TS_{11-13}}^{\mathbf{m}}$) are still


DOI: 10.1021/acscatal.8b03146
ACS Catal. 2018, 8, 10606−10618

more favorable than that for directly forming **Rh15$^{m}$** and **Ir15$^{m}$** (corresponding Rh and Ir complexes of **15$^{m}$**) and their isomers.

With the active species 4-BPin-($^{iPr}$PNP)CoBPin, we calculated this process by optimizing corresponding species **TS$_{11-13}^{BPin}$** and **13$^{BPin}$** with ωB97XD/BS4 (LANL2DZ for Co and 6-31G* for the others). The same method was employed to recalculate **TS$_{11-13}$** and **13** for consistency. At the level of ωB97XD/Def2TZVP(SMD)//ωB97XD/BS4, **TS$_{11-13}$**, **13**, **TS$_{11-13}^{BPin}$**, and **13$^{BPin}$** are 24.2[8.2](23.0), 21.9[6.9](22.0), 23.8[8.2](22.8), and 21.6[7.1](21.7) kcal/mol, respectively. Although the barrier for **TS$_{11-13}^{BPin}$** is slightly lower than that for **TS$_{11-13}$** in free energy, they are the same in enthalpy, and the former is slightly higher than the latter by 0.05 kcal/mol in SCF energy. Furthermore, as shown by Table 2 and corresponding discussions in the following section, the relative energies of **TS$_{11-13}^{BPin}$** and **TS$_{11-13}$** depend on selected calculation methods. The experimental observations that the C−H oxidative addition with 4-BPin-($^{iPr}$PNP)CoBPin is slower than that with ($^{iPr}$PNP)CoBPin[30] may be explained by these differences.

**Table 2. Calculated Barriers (kcal/mol) for Transition States TS$_{11-13}$ and TS$_{18-19}$ Relative to Separate 11 and C$_6$H$_6$ Using Different Functionals and Basis Sets**

| | TS$_{11-13}$ | TS$_{18-19}$ |
|---|---|---|
| ωB97XD/Def2TZVP(SMD)//ωB97XD/BS1 | 24.2 | 25.2 |
| M06/Def2TZVP(SMD)//M06/BS1 | 30.1 | 30.7 |
| B3LYP/Def2TZVP(SMD)//B3LYP/BS1 | 43.0 | 44.5 |
| B3LYP(GD3BJ)/Def2TZVP(SMD)//B3LYP(GD3BJ)/BS1 | 25.8 | 27.2 |
| M06L/Def2TZVP(SMD)//M06L/BS1 | 26.5 | 26.4 |
| ωB97XD/Def2TZVP(SMD)//ωB97XD/BS2 | 23.5 | 25.0 |
| ωB97XD/Def2TZVP(SMD)//ωB97XD/BS4[a] | 24.2 | 26.0 |
| ωB97XD/Def2TZVP(SMD)//ωB97XD/BS5[b] | 24.7 | 25.9 |
| M06/Def2TZVP(SMD)//M06/BS5[b] | 30.4 | 32.3 |
| B971/Def2TZVP(SMD)//B971/BS5[b] | 36.6 | 38.8 |
| TPSS/Def2TZVP(SMD)//TPSS/BS5[b] | 34.8 | 36.1 |
| TPSS/Def2TZVP(SMD)//TPSS/BS1 | 34.8 | 35.8 |

[a]Co uses LANL2DZ and the others use 6-31G* in BS4. [b]Co uses 6-31+G* and the others use 6-31G* in BS5.

**3.3. Reductive Elimination of B−C Bond to Form PhBPin.** From the C$_6$H$_6$ addition product **13**, the calculated energy profiles for the reductive elimination of the B−C bond to generate the borylation product PhBPin are shown in Figure 6. By beginning at complex **13**, where the pincer is folded and C$_6$H$_5$, H, and BPin are in the opposite *fac* site, the H and BPin groups rotate via transition state **TS$_{13-14}$** to form complex **14**, which adopts a distorted octahedral geometry where C$_6$H$_5$, H, BPin, and the pyridine ligands are in the same plane and the P−Co−P angle begins to open. Then, the P arm in blue tips up and the pincer unfolds into its mer site to form **15**, where the Ph and BPin groups are trans. Subsequently, the HBPin group dissociates from **15** to form a four-coordinated Co-phenyl complex **16**, followed by the reassociation of HBPin to generate complex **17** where the Ph and BPin groups are in cis positions (alternative dissociation/reassociation route are possible but were not investigated). For the vibrational modes of transition states **TS$_{15-16}$** and **TS$_{16-17}$**, in addition to the oxidation and reductive elimination of HBPin, the Ph groups are also rotating around Co toward or away from the trans position of the N atom. From complex **17** where the two five-membered phosphine rings of the pincer ligand are folded in different directions, the P arm in blue then flips down to afford complex **18**. In **18**, the Ph and BPin groups are in cis positions, from which they proceed through a reductive elimination transition state **TS$_{18-19}$** to form complex **19**, followed by the release of the product PhBPin to generate a Co−hydride complex **20**. The transition state **TS$_{18-19}$** corresponds to the reductive elimination of PhBPin and the rotation of H atom around Co.

Due to the release of steric effects between the ligands, complex **14** is more stable than **13** by 3.1 kcal/mol and complex **15** is more stable than **14** by 2.0 kcal/mol. Moreover, complex **17** is more stable than **15** by 6.8 kcal/mol. According to Figure 6, the reductive elimination processes are very favorable. The formations of Co(I) complexes **16** and **20** from their corresponding Co(III) complexes **15** and **18**, respectively, are favorable by releasing more than 9 kcal/mol. Overall, the generated PhBPin and complex **20** are lower than complex **13** by 26.5 kcal/mol, and they are also lower than separate reactants (C$_6$H$_6$ and **11**) by 3.5 kcal/mol. Thus, the reductive elimination process is thermodynamically favorable, which drives the reaction to produce PhBPin.

In comparison with the oxidative addition process in Figure 5, the reductive elimination process in Figure 6 appears to have the rate-determining step, as several transition states involved in Figure 6 (**TS$_{13-14}$**, **TS$_{14-15}$**, **TS$_{15-16}$**, **TS$_{16-17}$**, and **TS$_{18-19}$**) are a little higher than the C−H oxidative-addition transition state **TS$_{11-13}$**. The same conclusion was also obtained by using the experimentally proposed active species 4-BPin-($^{iPr}$PNP)-CoBPin, as the barrier of **TS$_{11-13}^{BPin}$** (23.8[8.2](22.8) kcal/mol) for the C−H oxidative addition is still lower than that of **TS$_{18-19}^{BPin}$** (25.7[9.7](23.0) kcal/mol) for the reductive elimination at the level of ωB97XD/Def2TZVP-(SMD)//ωB97XD/BS4. These results appear to be inconsistent with the experimental observations that the C−H oxidative addition was indicated to be the rate-determining step for the borylation of 2,6-lutidine with $B_2Pin_2$.[30] Of course, the differences between these barriers are small and the transition states involved in Figure 6 could adopt other lower-barrier conformations due to the flexibility of ligands, in particular the rotations of iPr groups and the orientations of phosphine ligands. Here, we hesitate to try to find all possible conformations because of the large computation cost and because we could not trust such small differences. To support this postulation, a similar reductive elimination pathway was calculated by using model systems (Figure S17 in SI15). The results show that the reductive elimination transition state **TS$_{18-19}^{m}$** (corresponding to **TS$_{18-19}$**) is the highest one among these transition states. However, **TS$_{18-19}^{m}$** is slightly lower by 0.5 kcal/mol than the C−H oxidative addition transition state **TS$_{11-13}^{m}$**. Thus, for the model system, the oxidative addition step is the rate-determining step. To further explore the effects of functionals and basis sets, calculations were conducted for these two important transition states **TS$_{11-13}$** (the oxidative addition transition state) and **TS$_{18-19}$** (the reductive elimination transition state) by employing several different DFT functionals and basis sets (Table 2). Although the barriers for **TS$_{18-19}$** are predicted to be slightly higher than that for **TS$_{11-13}$** with most of these tested methods, **TS$_{18-19}$** is lower than **TS$_{11-13}$** with M06L. In addition, the results at the level of M06/Def2TZVP(SMD)//M06/BS1 are very close with a difference of only 0.6 kcal/mol. Thus, the choice of


DOI: 10.1021/acscatal.8b03146
ACS Catal. 2018, 8, 10606−10618

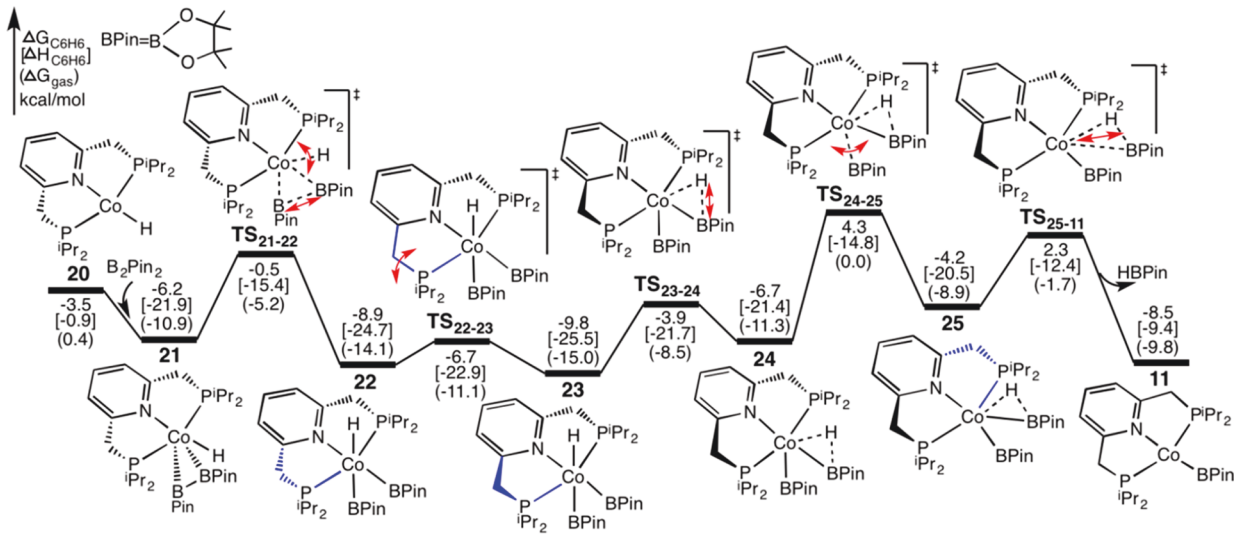


**Figure 7.** Calculated energy profiles for the regeneration of ($^{iPr}$PNP)CoBPin (**11**) from ($^{iPr}$PNP)CoH (**20**) and $B_2Pin_2$. Optimized geometries of these species are shown in SI16.

functional could be a source of this small inconsistency. Considering that the C−H oxidative addition is the rate-determining step, the overall barrier for the reaction is 24.2 kcal/mol from **11** to $\mathbf{TS_{11-13}}$. Consistent with the calculated barrier, the reaction was observed to occur at 80 °C for 24 h with the isolated yield of 87% by employing a 20:1 ration of arene to $B_2Pin_2$ in the reported experiments.[28]

From complex **13**, the barriers for the reductive elimination of the C−H bond via $\mathbf{TS_{11-13}}$, the reductive elimination of the B−H bond via $\mathbf{TS_{15-16}}$, and the reductive elimination of the B−C bond via $\mathbf{TS_{18-19}}$ are 1.2, 5.8, and 2.2 kcal/mol, respectively. Furthermore, their corresponding thermodynamics are −23.0, −14.7, and −26.5 kcal/mol for the formations of **11** and $C_6H_6$, the formations of **16** and HBPin, and the formations of **20** and PhBPin. Thus, the reductive elimination of the B−C bond is the most favorable process, which drives the reaction forward to produce PhBPin, while the reductive eliminations of the C−H and B−H bond are considered to be reversible.

The barriers for the ring "flipping" transition states $\mathbf{TS_{14-15}}^{m}$ and $\mathbf{TS_{17-18}}^{m}$, relative to separate $C_6H_6$ and $\mathbf{11}^{m}$, are 12.7 and −2.3 kcal/mol (Figure S17), which are lower than the corresponding (full system) transition states $\mathbf{TS_{14-15}}$ and $\mathbf{TS_{17-18}}$ in Figure 6, as there is less steric clashing between the substituents on the phosphine ligands in the model systems. In addition to the pathway shown in Figure 6, several other possibilities were considered by using model systems and found to be less favorable (see SI15): direct reductive elimination of the B−C bond from the oxidative addition product $\mathbf{13}^{m}$ (Figure S18), reductive elimination through an isomer of the $\mathbf{TS_{18-19}}^{m}$ with two phosphine ligands in different directions (Figure S19(A)), reductive elimination with the assistance of HBeg (Figure S19(B)), reductive elimination from the $C_6H_6$ oxidative addition product where the cleaved $C_6H_5$ and H are in cis positions (Figure S19(C)), reductive elimination via the dissociation of one phosphine ligand (Figure S19(D)), and reductive elimination from the oxidative addition product from $B_2eg_2$ and the Co(I)−Ph complex (Figure S20). With the experimentally reported systems, the process for the reductive elimination of the B−C bond to generate the borylated product PhBPin through the direct reductive elimination from **13** was further calculated to be unlikely, as the barrier for $\mathbf{TS_{13-20}}$ is very high, 38.4[23.6](36.3) kcal/mol relative to separated $C_6H_6$ and **11** (Figure S21). In addition, another possible pathway for the oxidative addition of $C_6H_6$ to the Co(I)−H complex $\mathbf{20}^{m}$ was also considered (Figure S22), but it was less favorable thermodynamically and kinetically than the oxidative addition of $B_2eg_2$ to regenerate the active species (Figure S24 in SI17).

At the level of ωB97XD/Def2TZVP-(SMD)//ωB97XD/BS4, $\mathbf{TS_{18-19}}$, **20**, $\mathbf{TS_{18-19}}^{BPin}$, and $\mathbf{20}^{BPin}$ are 26.0[9.7](23.3), −3.2[−0.8](2.2), 25.7[9.7](23.0), and −5.2[−1.0](0.2) kcal/mol, respectively, where $\mathbf{20}^{BPin}$ and $\mathbf{TS_{18-19}}^{BPin}$ are the active species 4-BPin-($^{iPr}$PNP)CoBPin and its corresponding transition state. Accordingly, the reductive elimination process with 4-BPin-($^{iPr}$PNP)CoBPin is more favorable than that with ($^{iPr}$PNP)CoBPin both kinetically and thermodynamically.

**3.4. Regeneration of ($^{iPr}$PNP)CoBPin.** In the presence of $B_2Pin_2$, the active species ($^{iPr}$PNP)CoBPin (**11**) can be regenerated from ($^{iPr}$PNP)CoH (**20**) by following the pathway shown in Figure 7. Coordination of $B_2Pin_2$ to **20** gives complex **21**, in which the B−B bond is parallel with the N−Co−H axis, is followed by transition state $\mathbf{TS_{21-22}}$ corresponding to simultaneous cleavage of the B−B bond and rotation of the Co−H bond to generate an octahedral complex **22**. Subsequently, the $sp^3$-C of the phosphine ring in blue flips up via transition state $\mathbf{TS_{22-23}}$ to form complex **23**. Like the dihydride cobalt complexes in Figure 2, complex **23**, where the two five-membered rings are folded in different directions, is slightly more stable than complex **22** where the two five-membered rings are folded in the same direction. Then, through transition state $\mathbf{TS_{23-24}}$, in which the H and BPin on Co are moving toward each other, and transition state $\mathbf{TS_{24-25}}$, in which BPin rotated and forms the new H−B bond. Finally, HBPin dissociates from **25** via transition state $\mathbf{TS_{25-11}}$ to regenerate the active species **11**. An alternative pathway for the generation of **11** from **25** via an intermediate that is formed from **25** by flipping up the $sp^3$-C of the phosphine ring in blue is slightly less favorable, and the transition state for the dissociation of HBPin from this intermediate is higher than $\mathbf{TS_{25-11}}$ by 0.7 kcal/mol. As shown in Figure 7, the formation


DOI: 10.1021/acscatal.8b03146
ACS Catal. 2018, 8, 10606−10618

of **11** with releasing HBPin from **20** and $B_2Pin_2$ is favorable thermodynamically and kinetically; the rate-determining barrier for this process is only 14.1 kcal/mol ($\mathbf{TS_{24-25}}$ relative to **23**).

The pathways discussed above are consistent with those for the model systems (SI17). In the model system several less favorable alternative paths were explored: formation of an isomer of **21**, in which the B−B bond is parallel with the P−Co−P axis, formation of **24** from **22**, in which the H and Beg on Co first move toward each other, followed by the $sp^3$-C of one phosphine ring fliping up, formation of **25** from **24**, in which the $sp^3$-C of one phosphine ring first flips up to generate an intermediate with two phosphine rings bending in the same direction, and the pathway with one phosphine ligand dissociated (Figure S25 in SI17).

## 4. CONCLUSIONS

Density functional theory calculations on C−H borylation catalyzed by cobalt pincer complexes with $C_6H_6$ and $B_2Pin_2$ as substrates predict a mechanism involving three distinct steps: oxidative addition of $C_6H_6$, reductive elimination PhBPin, and regeneration of ($^{iPr}$PNP)CoBPin. The *trans*-($^{iPr}$PNP)-$CoH_2$(BPin) complex was experimentally observed as a resting state in the borylation of five-membered heteroarenes. Starting from this complex, the active species, ($^{iPr}$PNP)CoBPin, is generated by rearrangement to the cis isomer and reductive elimination of $H_2$. The isomerization pathway is similar to the well-known Berry pseudorotation mechanism with the $H^1$BPin group acting as a unit in a 5-coordinate Co. The metal−ligand cooperative mechanism based on the ligand's aromatization/dearomatization, which is widely proposed to explain the catalytic reactions by the PNP pincer ligated to heavier metals, is computed to be less favorable for this system. Additionally, the 4-BPin-($^{iPr}$PNP)Co($N_2$)BPin complex, which can easily release $N_2$ to form the active species, was identified as the resting state in the catalytic borylation of arene substrates. The lowest barrier for oxidative addition of $C_6H_6$ forms a complex with a distorted PNP ligand, which rearranges to a more stable complex via dissociation and reassociation of HBPin. Possible $\sigma$-bond metathesis pathways are predicted to be unlikely for this Co(I) complex. Reductive elimination of PhBPin is thermodynamically favorable and drives the reaction forward. The regeneration of the active species was found to proceed through the oxidative addition of $B_2Pin_2$ and reductive elimination of HBPin. In the overall reaction, the flipping up and down of the $sp^3$-C of the five-membered phosphine rings, which connects the species with two phosphine rings folded in the same direction and that with them folded in different directions, is found to play important roles in the catalytic process, as this motion releases steric crowding within the PNP ligand and opens Co coordination space. This investigation provides some guidance for further understanding of important features of pincer ligands with first-transition-row metals that differ from those in heavier metal complexes.

## ■ ASSOCIATED CONTENT

### Supporting Information

The Supporting Information is available free of charge on the ACS Publications website at DOI: 10.1021/acscatal.8b03146.

Verification of ground states of four-coordinate cobalt species; optimized geometries of some species involved in Figure 2; the superimposed structures of the optimized geometry of **2** and its X-ray crystal structure; an alternative pathway for the formation of **4** from **2**; formation of the isomer of **9**; isomerization of **4** to its isomer; results for the release of $H_2$ from the trans-dihydride Co-complex with model systems; verification of $\omega$B97XD/Def2TZVP(SMD)//$\omega$B97XD/BS4; optimized geometries of transition states for the release of $H_2$ from $\mathbf{2^{Ir}}$, $\mathbf{2^{Ph}}$, $\mathbf{2^{Ir-Ph}}$, and $\mathbf{2^{Ir-Ph-tBu}}$; a possible pathway for the formation of the active species from the catalyst precursor with model systems; alternative pathways for the addition of $C_6H_6$ to the cobalt boryl species with model systems; comparisons of transition state $\mathbf{TS_{11-13}}$ and that for the formation of **15** and its isomer; addition of $C_6H_6$ to corresponding Rh and Ir complexes; optimized geometries for the species in Figure 6 in the text; results for the reductive elimination of the B−C bond with model systems; optimized geometries of the species in Figure 7; results for the regeneration of the active species with model systems (PDF)

Cartesian coordinates and energies of the species involved in the text (PDF)

## ■ AUTHOR INFORMATION


### Corresponding Author

*mbhall@tamu.edu.

### ORCID

Paul J. Chirik: 0000-0001-8473-2898

Michael B. Hall: 0000-0003-3263-3219


### Notes

The authors declare no competing financial interest.

## ■ ACKNOWLEDGMENTS

L.H. and M.B.H. thank the National Science Foundation (CHE-1300787 and 1664866) and the Welch Foundation (A-0648) for financial support and the Texas A&M High Performance Research Computing Center and the Laboratory for Molecular Simulation for providing computing resources. J.V.O. and P.J.C. would like to thank the National Institutes of Health (1R01GM121441-01).

## ■ REFERENCES


(1) Mkhalid, I. A. I.; Barnard, J. H.; Marder, T. B.; Murphy, J. M.; Hartwig, J. F. C-H Activation for the Construction of C-B Bonds. *Chem. Rev.* **2010**, *110*, 890−931.

(2) Hartwig, J. F. Regioselectivity of the Borylation of Alkanes and Arenes. *Chem. Soc. Rev.* **2011**, *40*, 1992−2002.

(3) Hartwig, J. F. Borylation and Silylation of C-H Bonds: A Platform for Diverse C-H Bond Functionalizations. *Acc. Chem. Res.* **2012**, *45*, 864−873.

(4) Li, Q.; Driess, M.; Hartwig, J. F. Iridium-Catalyzed Regioselective Silylation of Aromatic and Benzylic C-H Bonds Directed by a Secondary Amine. *Angew. Chem., Int. Ed.* **2014**, *53*, 8471−8474.

(5) Ishiyama, T.; Miyaura, N. Transition Metal-Catalyzed Borylation of Alkanes and Arenes via C-H Activation. *J. Organomet. Chem.* **2003**, *680*, 3−11.

(6) Ros, A.; Fernandez, R.; Lassaletta, J. M. Functional Group Directed C-H Borylation. *Chem. Soc. Rev.* **2014**, *43*, 3229−3243.

(7) Thomas, R. L.; Souza, F. E. S.; Marder, T. B. Highly Efficient Monophosphine Platinum Catalysts for Alkyne Diboration. *J. Chem. Soc.-Dalton Trans.* **2001**, 1650−1656.

(8) Lee, C. I.; Shih, W. C.; Zhou, J.; Reibenspies, J. H.; Ozerov, O. V. Synthesis of Triborylalkenes from Terminal Alkynes by Iridium-

Catalyzed Tandem C-H Borylation and Diboration. *Angew. Chem., Int. Ed.* **2015**, *54*, 14003−14007.
(9) Kubota, K.; Iwamoto, H.; Yamamoto, E.; Ito, H. Silicon-Tethered Strategy for Copper(I)-Catalyzed Stereo- and Regioselective Alkylboration of Alkynes. *Org. Lett.* **2015**, *17*, 620−623.
(10) Nakagawa, N.; Hatakeyama, T.; Nakamura, M. Iron-Catalyzed Diboration and Carboboration of Alkynes. *Chem. - Eur. J.* **2015**, *21*, 4257−4261.
(11) Itoh, T.; Shimizu, Y.; Kanai, M. Ligand-Enabled, Copper-Catalyzed Regio- and Stereoselective Synthesis of Trialkylsubstituted Alkenylboronates from Unactivated Internal Alkynes. *J. Am. Chem. Soc.* **2016**, *138*, 7528−7531.
(12) Cook, A. K.; Schimler, S. D.; Matzger, A. J.; Sanford, M. S. Catalyst-Controlled Selectivity in the C-H Borylation of Methane and Ethane. *Science* **2016**, *351*, 1421−1424.
(13) Smith, K. T.; Berritt, S.; Gonzalez-Moreiras, M.; Ahn, S.; Smith, M. R.; Baik, M. H.; Mindiola, D. J. Catalytic Borylation of Methane. *Science* **2016**, *351*, 1424−1427.
(14) Chirik, P. J. Iron- and Cobalt-Catalyzed Alkene Hydrogenation: Catalysis with Both Redox-Active and Strong Field Ligands. *Acc. Chem. Res.* **2015**, *48*, 1687−1695.
(15) Holland, P. L. Distinctive Reaction Pathways at Base Metals in High-Spin Organometallic Catalysts. *Acc. Chem. Res.* **2015**, *48*, 1696−1702.
(16) Waltz, K. M.; He, X. M.; Muhoro, C.; Hartwig, J. F. Hydrocarbon Functionalization by Transition-Metal Boryls. *J. Am. Chem. Soc.* **1995**, *117*, 11357−11358.
(17) Légaré, M. A.; Courtemanche, M. A.; Rochette, E.; Fontaine, F. G. Metal-free Catalytic C-H Bond Activation and Borylation of Heteroarenes. *Science* **2015**, *349*, 513−516.
(18) Bose, S. K.; Marder, T. B. A Leap Ahead for Activating C-H Bonds. *Science* **2015**, *349*, 473−474.
(19) Légaré, M. A.; Rochette, E.; Lavergne, J. L.; Bouchard, N.; Fontaine, F. G. Bench-Stable Frustrated Lewis Pair Chemistry: Fluoroborate Salts as Precatalysts for the C-H Borylation of Heteroarenes. *Chem. Commun.* **2016**, *52*, 5387−5390.
(20) Chernichenko, K.; Lindqvist, M.; Kótai, B.; Nieger, M.; Sorochkina, K.; Pápai, I.; Repo, T. Metal-Free sp(2)-C-H Borylation as a Common Reactivity Pattern of Frustrated 2-Aminophenylboranes. *J. Am. Chem. Soc.* **2016**, *138*, 4860−4868.
(21) Iashin, V.; Chernichenko, K.; Pápai, I.; Repo, T. Atom-Efficient Synthesis of Alkynylfluoroborates Using BF3-Based Frustrated Lewis Pairs. *Angew. Chem., Int. Ed.* **2016**, *55*, 14146−14150.
(22) Mazzacano, T. J.; Mankad, N. P. Base Metal Catalysts for Photochemical C-H Borylation That Utilize Metal-Metal Cooperativity. *J. Am. Chem. Soc.* **2013**, *135*, 17258−17261.
(23) Parmelee, S. R.; Mazzacano, T. J.; Zhu, Y. Q.; Mankad, N. P.; Keith, J. A. A Heterobimetallic Mechanism for C-H Borylation Elucidated from Experimental and Computational Data. *ACS Catal.* **2015**, *5*, 3689−3699.
(24) Mankad, N. P. Non-Precious Metal Catalysts for C-H Borylation Enabled by Metal-Metal Cooperativity. *Synlett* **2014**, *25*, 1197−1201.
(25) Dombray, T.; Werncke, C. G.; Jiang, S.; Grellier, M.; Vendier, L.; Bontemps, S.; Sortais, J. B.; Sabo-Etienne, S.; Darcel, C. Iron-Catalyzed C-H Borylation of Arenes. *J. Am. Chem. Soc.* **2015**, *137*, 4062−4065.
(26) Mazzacano, T. J.; Mankad, N. P. Thermal C-H Borylation Using a CO-free Iron Boryl Complex. *Chem. Commun.* **2015**, *51*, 5379−5382.
(27) Yoshigoe, Y.; Kuninobu, Y. Iron-Catalyzed Ortho-Selective C-H Borylation of 2-Phenylpyridines and Their Analogs. *Org. Lett.* **2017**, *19*, 3450−3453.
(28) Obligacion, J. V.; Semproni, S. P.; Chirik, P. J. Cobalt-Catalyzed C-H Borylation. *J. Am. Chem. Soc.* **2014**, *136*, 4133−4136.
(29) Schaefer, B. A.; Margulieux, G. W.; Small, B. L.; Chirik, P. J. Evaluation of Cobalt Complexes Bearing Tridentate Pincer Ligands for Catalytic C-H Borylation. *Organometallics* **2015**, *34*, 1307−1320.
(30) Obligacion, J. V.; Semproni, S. P.; Pappas, I.; Chirik, P. J. Cobalt-Catalyzed C(sp(2))-H Borylation: Mechanistic Insights Inspire Catalyst Design. *J. Am. Chem. Soc.* **2016**, *138*, 10645−10653.
(31) Palmer, W. N.; Obligacion, J. V.; Pappas, I.; Chirik, P. J. Cobalt-Catalyzed Benzylic Borylation: Enabling Polyborylation and Functionalization of Remote, Unactivated C(sp(3))-H Bonds. *J. Am. Chem. Soc.* **2016**, *138*, 766−769.
(32) Leonard, N. G.; Bezdek, M. J.; Chirik, P. J. Cobalt-Catalyzed C(sp(2))-H Borylation with an Air-Stable, Readily Prepared Terpyridine Cobalt(II) Bis(acetate) Precatalyst. *Organometallics* **2017**, *36*, 142−150.
(33) Obligacion, J. V.; Bezdek, M. J.; Chirik, P. J. C(sp(2))-H Borylation of Fluorinated Arenes Using an Air-Stable Cobalt Precatalyst: Electronically Enhanced Site Selectivity Enables Synthetic Opportunities. *J. Am. Chem. Soc.* **2017**, *139*, 2825−2832.
(34) Obligacion, J. V.; Chirik, P. J. Mechanistic Studies of Cobalt-Catalyzed C(sp(2))-H Borylation of Five-Membered Heteroarenes with Pinacolborane. *ACS Catal.* **2017**, *7*, 4366−4371.
(35) Ren, H. L.; Zhou, Y. P.; Bai, Y. P.; Cui, C. M.; Driess, M. Cobalt-Catalyzed Regioselective Borylation of Arenes: N-Heterocyclic Silylene as an Electron Donor in the Metal-Mediated Activation of C-H Bonds. *Chem. - Eur. J.* **2017**, *23*, 5663−5667.
(36) Furukawa, T.; Tobisu, M.; Chatani, N. Nickel-Catalyzed Borylation of Arenes and Indoles via C-H Bond Cleavage. *Chem. Commun.* **2015**, *51*, 6508−6511.
(37) (a) Zhang, H.; Hagihara, S.; Itami, K. Aromatic C-H Borylation by Nickel Catalysis. *Chem. Lett.* **2015**, *44*, 779−781. (b) Furukawa, T.; Tobisu, M.; Chatani, N. Nickel-Catalyzed Borylation of Arenes and Indoles via C-H Bond Cleavage. *Chem. Commun.* **2015**, *51*, 6508−6511.
(38) Tamura, H.; Yamazaki, H.; Sato, H.; Sakaki, S. Iridium-Catalyzed Borylation of Benzene with Diboron. Theoretical Elucidation of Catalytic Cycle Including Unusual Iridium(V) Intermediate. *J. Am. Chem. Soc.* **2003**, *125*, 16114−16126.
(39) (a) Webster, C. E.; Fan, Y. B.; Hall, M. B.; Kunz, D.; Hartwig, J. F. Experimental and Computational Evidence for a Boron-Assisted, Sigma-Bond Metathesis Pathway for Alkane Borylation. *J. Am. Chem. Soc.* **2003**, *125*, 858−859. (b) Vastine, B.; Hall, M. B. The Molecular and Electronic Structure of Carbon−Hydrogen Bond Activation and Transition Metal Assisted Hydrogen Transfer *Coord. Coord. Chem. Rev.* **2009**, *253*, 1202−1218.
(40) Sumimoto, M.; Iwane, N.; Takahama, T.; Sakaki, S. Theoretical Study of Trans-Metalation Process in Palladium-Catalyzed Borylation of Iodobenzene with Diboron. *J. Am. Chem. Soc.* **2004**, *126*, 10457−10471.
(41) Boller, T. M.; Murphy, J. M.; Hapke, M.; Ishiyama, T.; Miyaura, N.; Hartwig, J. F. Mechanism of the Mild Functionalization of Arenes by Diboron Reagents Catalyzed by Iridium Complexes. Intermediacy and Chemistry of Bipyridine-Ligated Iridium Trisboryl Complexes. *J. Am. Chem. Soc.* **2005**, *127*, 14263−14278.
(42) Hartwig, J. F.; Cook, K. S.; Hapke, M.; Incarvito, C. D.; Fan, Y. B.; Webster, C. E.; Hall, M. B. Rhodium Boryl Complexes in the Catalytic, Terminal Functionalization of Alkanes. *J. Am. Chem. Soc.* **2005**, *127*, 2538−2552.
(43) Dang, L.; Lin, Z. Y.; Marder, T. B. DFT Studies on the Borylation of Alpha,beta-Unsaturated Carbonyl Compounds Catalyzed by Phosphine Copper(I) Boryl Complexes and Observations on the Interconversions Between O- and C-Bound Enolates of Cu, B, and Si. *Organometallics* **2008**, *27*, 4443−4454.
(44) Olsson, V. J.; Szabo, K. J. Functionalization of Unactivated Alkenes through Iridium-Catalyzed Borylation of Carbon-Hydrogen Bonds. Mechanism and Synthetic Applications. *J. Org. Chem.* **2009**, *74*, 7715−7723.
(45) Sawyer, K. R.; Cahoon, J. F.; Shanoski, J. E.; Glascoe, E. A.; Kling, M. F.; Schlegel, J. P.; Zoerb, M. C.; Hapke, M.; Hartwig, J. F.; Webster, C. E.; Harris, C. B. Time-resolved IR Studies on the Mechanism for the Functionalization of Primary C-H Bonds by Photoactivated Cp*W(CO)(3)(Bpin). *J. Am. Chem. Soc.* **2010**, *132*, 1848−1859.


DOI: 10.1021/acscatal.8b03146
*ACS Catal.* 2018, 8, 10606−10618

(46) Lam, W. H.; Lam, K. C.; Lin, Z. Y.; Shimada, S.; Perutz, R. N.; Marder, T. B. Theoretical Study of Reaction Pathways for the Rhodium Phosphine-Catalysed Borylation of C-H Bonds with Pinacolborane. *Dalton Trans* **2004**, 1556−1562.
(47) Vanchura, B. A.; Preshlock, S. M.; Roosen, P. C.; Kallepalli, V. A.; Staples, R. J.; Maleczka, R. E.; Singleton, D. A.; Smith, M. R. Electronic Effects in Iridium C-H Borylations: Insights from Unencumbered Substrates and Variation of Boryl Ligand Substituents. *Chem. Commun.* **2010**, *46*, 7724−7726.
(48) Wei, C. S.; Jimenez-Hoyos, C. A.; Videa, M. F.; Hartwig, J. F.; Hall, M. B. Origins of the Selectivity for Borylation of Primary over Secondary C-H Bonds Catalyzed by Cp*-Rhodium Complexes. *J. Am. Chem. Soc.* **2010**, *132*, 3078−3091.
(49) Roosen, P. C.; Kallepalli, V. A.; Chattopadhyay, B.; Singleton, D. A.; Maleczka, R. E.; Smith, M. R. Outer-Sphere Direction in Iridium C-H Borylation. *J. Am. Chem. Soc.* **2012**, *134*, 11350−11353.
(50) Green, A. G.; Liu, P.; Merlic, C. A.; Houk, K. N. Distortion/Interaction Analysis Reveals the Origins of Selectivities in Iridium-Catalyzed C-H Borylation of Substituted Arenes and 5-Membered Heterocycles. *J. Am. Chem. Soc.* **2014**, *136*, 4575−4583.
(51) Larsen, M. A.; Hartwig, J. F. Iridium-Catalyzed C-H Borylation of Heteroarenes: Scope, Regioselectivity, Application to Late-Stage Functionalization, and Mechanism. *J. Am. Chem. Soc.* **2014**, *136*, 4287−4299.
(52) Larsen, M. A.; Wilson, C. V.; Hartwig, J. F. Iridium-Catalyzed Borylation of Primary Benzylic C-H Bonds without a Directing Group: Scope, Mechanism, and Origins of Selectivity. *J. Am. Chem. Soc.* **2015**, *137*, 8633−8643.
(53) Haines, B. E.; Saito, Y.; Segawa, Y.; Itami, K.; Musaev, D. G. Flexible Reaction Pocket on Bulky Diphosphine-Ir Complex Controls Regioselectivity in para-Selective C-H Borylation of Arenes. *ACS Catal.* **2016**, *6*, 7536−7546.
(54) Zhu, L.; Qi, X. T.; Li, Y. Z.; Duan, M.; Zou, L. F.; Bai, R. P.; Lan, Y. Ir(III)/Ir(V) or Ir(I)/Ir(III) Catalytic Cycle? Steric-Effect-Controlled Mechanism for the para-C-H Borylation of Arenes. *Organometallics* **2017**, *36*, 2107−2115.
(55) Semproni, S. P.; Milsmann, C.; Chirik, P. J. Four-Coordinate Cobalt Pincer Complexes: Electronic Structure Studies and Ligand Modification by Homolytic and Heterolytic Pathways. *J. Am. Chem. Soc.* **2014**, *136*, 9211−9224.
(56) Gunanathan, C.; Milstein, D. Bond Activation and Catalysis by Ruthenium Pincer Complexes. *Chem. Rev.* **2014**, *114*, 12024−12087.
(57) Zell, T.; Milstein, D. Hydrogenation and Dehydrogenation Iron Pincer Catalysts Capable of Metal Ligand Cooperation by Aromatization/Dearomatization. *Acc. Chem. Res.* **2015**, *48*, 1979−1994.
(58) Li, H.; Hall, M. B. Computational Mechanistic Studies on Reactions of Transition Metal Complexes with Noninnocent Pincer Ligands: Aromatization Dearomatization or Not. *ACS Catal.* **2015**, *5*, 1895−1913.
(59) Li, H.; Hall, M. B. Mechanism of the Formation of Carboxylate from Alcohols and Water Catalyzed by a Bipyridine-Based Ruthenium Complex: A Computational Study. *J. Am. Chem. Soc.* **2014**, *136*, 383−395.
(60) Chai, J.-D.; Head-Gordon, M. Long-range Corrected Hybrid Density Functionals with Damped Atom-atom Dispersion Corrections. *Phys. Chem. Chem. Phys.* **2008**, *10*, 6615−6620.
(61) Dunning, T. H. Gaussian-basis Sets for Use in Correlated Molecular Calculations 0.1. the Atoms Boron Through Neon and Hydrogen. *J. Chem. Phys.* **1989**, *90*, 1007−1023.
(62) Weigend, F.; Ahlrichs, R. Balanced Basis Sets of Split Valence, Triple Zeta Valence and Quadruple Zeta Valence Quality for H to Rn: Design and Assessment of Accuracy. *Phys. Chem. Chem. Phys.* **2005**, *7*, 3297−3305.
(63) Marenich, A. V.; Cramer, C. J.; Truhlar, D. G. Universal Solvation Model Based on Solute Electron Density and on a Continuum Model of the Solvent Defined by the Bulk Dielectric Constant and Atomic Surface Tensions. *J. Phys. Chem. B* **2009**, *113*, 6378−6396.
(64) Hay, P. J.; Wadt, W. R. Ab Initio Effective Core Potentials for Molecular Calculations − Potentials for the Transition-Metal Atoms Sc to Hg. *J. Chem. Phys.* **1985**, *82*, 270−283.
(65) Andrae, D.; Häussermann, U.; Dolg, M.; Stoll, H.; Preuss, H. Energy-Adjusted Ab Initio Pseudopotentials for the 2nd and 3rd Row Transition-Elements. *Theor. Chim. Acta* **1990**, *77*, 123−141.
(66) Zhao, Y.; Truhlar, D. G. The M06 Suite of Density Functionals for Main Group Thermochemistry, Thermochemical Kinetics, Noncovalent Interactions, Excited States, and Transition Elements: Two New Functionals and Systematic Testing of Four M06-Class Functionals and 12 Other Functionals. *Theor. Chem. Acc.* **2008**, *120*, 215−241.
(67) Tao, J. M.; Perdew, J. P.; Staroverov, V. N.; Scuseria, G. E. Climbing the Density Functional Ladder: Nonempirical Meta-Generalized Gradient Approximation Designed for Molecules and Solids. *Phys. Rev. Lett.* **2003**, *91*, 146401.
(68) Grimme, S.; Ehrlich, S.; Goerigk, L. Effect of the Damping Function in Dispersion Corrected Density Functional Theory. *J. Comput. Chem.* **2011**, *32*, 1456−1465.
(69) Zhao, Y.; Truhlar, D. G. A New Local Density Functional for Main-Group Thermochemistry, Transition Metal Bonding, Thermochemical Kinetics, and Noncovalent Interactions. *J. Chem. Phys.* **2006**, *125*, 194101.
(70) Perdew, J. P.; Burke, K.; Ernzerhof, M. Generalized Gradient Approximation Made Simple. *Phys. Rev. Lett.* **1996**, *77*, 3865−3868.
(71) Frisch, M. J.; Trucks, G. W.; Schlegel, H. B.; Scuseria, G. E.; Robb, M. A.; Cheeseman, J. R.; Scalmani, G.; Barone, V.; Mennucci, B.; Petersson, G. A.; Nakatsuji, H.; Caricato, M.; Li, X.; Hratchian, H. P.; Izmaylov, A. F.; Bloino, J.; Zheng, G.; Sonnenberg, J. L.; Hada, M.; Ehara, M.; Toyota, K.; Fukuda, R.; Hasegawa, J.; Ishida, M.; Nakajima, T.; Honda, Y.; Kitao, O.; Nakai, H.; Vreven, T.; Montgomery, J. A., Jr.; Peralta, J. E.; Ogliaro, F.; Bearpark, M.; Heyd, J. J.; Brothers, E.; Kudin, K. N.; Staroverov, V. N.; Keith, T.; Kobayashi, R.; Normand, J.; Raghavachari, K.; Rendell, A.; Burant, J. C.; Iyengar, S. S.; Tomasi, J.; Cossi, M.; Rega, N.; Millam, J. M.; Klene, M.; Knox, J. E.; Cross, J. B.; Bakken, V.; Adamo, C.; Jaramillo, J.; Gomperts, R.; Stratmann, R. E.; Yazyev, O.; Austin, A. J.; Cammi, R.; Pomelli, C.; Ochterski, J. W.; Martin, R. L.; Morokuma, K.; Zakrzewski, V. G.; Voth, G. A.; Salvador, P.; Dannenberg, J. J.; Dapprich, S.; Daniels, A. D.; Farkas, O.; Foresman, J. B.; Ortiz, J. V.; Cioslowski, J.; Fox, D. J. *Gaussian 09*, Revision D01; Gaussian Inc., Wallingford CT, 2013.
(72) Manson, J.; Webster, C. E.; Pérez, L. M.; Hall, M. B.; *Jimp2* version 091, released on May 19, 2006; http://www.chem.tamu.edu/jimp2/index.html.
(73) Hall, M. B.; Fenske, R. F. Electronic Structure and Bonding in Methyl- and Perfluoromethyl(pentacarbonyl)manganese. *Inorg. Chem.* **1972**, *11*, 768−775.
(74) Bursten, B. E.; Jensen, J. R.; Fenske, R. F. An X$\alpha$ Optimized Atomic Orbital Basis. *J. Chem. Phys.* **1978**, *68*, 3320−3321.
(75) Berry, R. S. Correlation of Rates of Intramolecular Tunneling Process, With Application to Some Group-V Compounds. *J. Chem. Phys.* **1960**, *32*, 933−938.
(76) Xu, H.; Bernskoetter, W. H. Mechanistic Considerations for C−C Bond Reductive Coupling at a Cobalt(III) Center. *J. Am. Chem. Soc.* **2011**, *133*, 14956−14959.
(77) Ben-Ari, E.; Leitus, G.; Shimon, L. J. W.; Milstein, D. Metal-ligand Cooperation in C-H and H-2 Activation by an Electron-rich PNPIr(I) System: Facile Ligand Dearomatization-Aromatization as Key Steps. *J. Am. Chem. Soc.* **2006**, *128*, 15390−15391.


DOI: 10.1021/acscatal.8b03146
*ACS Catal.* 2018, 8, 10606−10618